

Combining a Data Driven and Mechanistic Model to Predict Capacity and Potential Curve-Degradation

Jochen Stadler,* Johannes Fath, Madeleine Ecker, and Arnulf Latz

This work compares a state of the art data-driven model to predict the state of health (SoH) in lithium ion batteries with a new prediction model based on the mechanistic framework. The mechanistic approach attributes the degradation to individual components such as loss of available capacity on each electrode as well as loss of cyclable lithium. By combining the mechanistic framework with data-driven models for the component losses based on a design of experiment, we achieve a cycle aging model that can predict capacity degradation as well as degradation-

induced changes to the discharge potential curve. Using this cycle aging model alongside with a semi-empirical calendar aging model, we present a holistic aging model that we validate on independent validation tests containing time-variant load profiles. While the purely data-driven model is better at predicting the SoH, the mechanistic model clearly has its advantages in a deeper understanding that can potentially enhance the current methods of tracking and updating the characteristic open-circuit voltage curve over lifetime.

1. Introduction

In addition to safety and energy content, improving the lifetime of lithium-ion batteries is an important research goal to increase the sustainability of this technology, and thus a key factor in the energy and mobility transition. To improve lifetime, aging of batteries needs to be understood and modeled through equations. There are different approaches in literature for this purpose. On the one hand, there are physico-chemical models that attempt to describe mass transport at different hierarchical levels. These models are widely applicable and can make an important contribution, especially in the design of new lithium-ion cells. However, they are also complex and require extensive parameterization.^[1,2]

On the other hand, there are data-driven models that attempt to find and parameterize as generalizable equations as possible based on extensive experiments. These models often provide a very accurate description of aging, but at the same time offer little insight into the underlying causes of degradation and have difficulties with any form of extrapolation.

In between these two approaches, there are methods that combine physically motivated equations with data-driven

approaches, known as semi-empirical models. One of these approaches is the mechanistic model, that was established by Dubarry et al.^[3] on the cornerstone of the differential voltage analysis (DVA or dU/dQ) developed by Bloom et al.^[4] The mechanistic model bases the capacity degradation as well as the changes in the open-circuit voltage of a lithium ion-battery on so called aging modes, that describe these changes as a physical interplay between the electrodes and the available amount of lithium ions. The mechanistic model has been a valuable analysis tool that contributed to clarify and describe, among other things, that individual aging modes can first run hidden without affecting the measurable capacity, and later become dominant and thus determine the following degradation trajectory, leading to a visible kink in the aging curve.^[5,6]

While the mechanistic model itself can be seen as a ultimate reduced-order physical model,^[6] it becomes a semi-empirical prediction model when it is paired with empirically parameterized equations to describe the aging modes over lifetime. Recently, such model approaches were presented for calendar aging^[7] as well as cycle aging.^[8]

However, to the best of our knowledge, no mechanistic aging model has been presented that combines calendar and cyclic modeling and can thus predict the aging behavior of any dynamic usage scenario.

In this work, we present a cycle aging model based on the mechanistic model approach that uses data-driven models of the aging modes to enable predictions of arbitrary usage profiles. We combine this cycle aging model with a literature-known semi-empirical calendar prediction model to obtain a comprehensive model and validate this model through independent validation tests. Furthermore, we compare the mechanistic approach with a conventional, purely data-driven cycle aging model, similar to the approach we have presented previously.^[9]

We mainly focus on the parameterization of the models, and the functional principle of the combined prediction. However, the interested reader can find a comprehensive analysis of the

J. Stadler, Dr. J. Fath, Dr. M. Ecker
Mercedes-Benz AG
Mercedesstr. 122, 70546 Stuttgart, Germany
E-mail: jochen.stadler@mercedes-benz.com

J. Stadler, Prof. A. Latz
Ulm University (UULM)
Albert-Einstein-Allee 47, 89081 Ulm, Germany

Prof. A. Latz
Helmholtz Institute Ulm (HIU)
Helmholtzstr. 11, 89081 Ulm, Germany

 Supporting information for this article is available on the WWW under https://doi.org/10.1002/batt.202400211

 © 2024 The Author(s). *Batteries & Supercaps* published by Wiley-VCH GmbH. This is an open access article under the terms of the Creative Commons Attribution License, which permits use, distribution and reproduction in any medium, provided the original work is properly cited.

underlying aging phenomena and dependencies in our previous works.^[9,10]

2. Experimental

2.1. Parameterization Data

For this work we use the aging experiment presented in Ref. [11]. We tested a total of 62 pouch-bag type lithium-ion cells with a nominal capacity of 43 Ah with graphite on the negative and a blend of $\text{Li}(\text{Ni}_{0.6}\text{Mn}_{0.2}\text{Co}_{0.2})\text{O}_2$ and $\text{Li}(\text{Ni}_{1/3}\text{Mn}_{1/3}\text{Co}_{1/3})\text{O}_2$ on the positive electrode. The electrolyte is based on ethylene carbonate/diethyl carbonate with LiPF_6 as conducting salt. To ensure high reproducibility we used cells manufactured on serial production devices and test each aging condition with two cells.

A cycle aging matrix, planned as a design of experiment, varied five aging factors temperature T, maximum and minimum state of charge SoC_{\max} and SoC_{\min} , charging power P_{CH} and ratio of full electrical driving EV_{ratio} , based on a common center point. This approach not only covers the isolated influence of the five factors, but also their interactions. One cycle consisted of a constant power charging with a defined P_{CH} to reach SoC_{\max} , followed by discharging to SoC_{\min} using a power profile that closely resembles real-world EV usage. Afterward, a charge-sustaining hybrid electric vehicle (HEV) power profile was used until the EV_{ratio} was met. The force was kept constant through spring-loaded steel jigs, climate chambers controlled the ambient temperature. Every two weeks, a reference parameter test (RPT) that contains CC-discharges at a C-Rate of 1 C and 0.1 C between 4.2 V and 2.5 V at 25 °C characterized the cell's electrical state.

The tests cover a charge throughput between 100 kWh and 350 kWh which corresponds to about 1200–4000 full equivalent cycles. For a more detailed description and analysis of the aging test, we refer to Refs. [11] and [10].

The calendar aging tests are further described in Supporting Information S1.

2.2. Validation Data

To validate the models' predictive performance, we set up an independent validation experiment that closely follows the parameterization experiment but includes increasingly difficult prediction tasks that are defined in Table 1. The cell-type, setup as well as cycle- and RPT-procedures are comparable to the

parameterization test. Again, each test conditions was tested with two cells.

- Test I repeats the center point of the parameterization experiment to verify reproducibility of the results.
- Test II uses a low SoC_{\min} to evaluate the models extrapolative performance to low SoC.
- Test III uses a different power profile to test whether the method of evaluating mean aging conditions on a cycle basis also works with different dynamics in the discharging profile. Figures S2 and S3 show the different distributions of the two discharge profiles.
- Test IV introduces time-variant aging conditions. While the values always stay within the parameterized model range, the validity of the damage accumulation approach is tested.
- Test V not only varies cycle aging conditions within the model range but also adds a storage sequence to the test procedure to validate the damage accumulation approach between cycle and calendar aging model.

The tests cover a charge throughput between 170 kWh and 350 kWh which corresponds to about 2000–4000 full equivalent cycles.

3. Modeling Methods and Parameterization

The following sections describe the workflow of the model parameterization, which is depicted in Figure 1. In brief, we first parameterize a purely empirical model to predict SoH_c , which we refer to as global SoH_c model. Here, the parameterization is straightforward, as we can directly use the measured C/10 capacities from the RPTs, subtract calendar aging and then optimize an empirical function to express SOH_{cyc} as function of the aging conditions. For predictions, we then use this empirical function in a damage accumulation approach, add calendar aging and can thereby estimate the SoH_c for any profile.

In comparison, we parameterize a hybrid mechanistic model. The mechanistic model physically describes the effect of the aging modes loss of cyclable lithium inventory (LLI), active material loss on negative (LAM_{NE}) and positive electrode (LAM_{PE}) and the spatial inhomogeneity of the lithium distribution across the electrodes (σ_{LLI}) on the cells capacity as well as the potential curve. These aging modes, which we also refer to as component losses, can be determined via dU/dQ -fitting from the measured C/10 potential curves. Pure cycle aging is achieved by partitioning LLI into a calendar and a cycle contribution. Then, similar to the global SoH_c model, an empirical approach expresses every component loss as a function of the aging conditions. We then

Table 1. Specified Aging Conditions for the validation experiments. Tests 4 and 5 change the specified aging conditions after every three sequences.							
Val. Test	Description	Temp. [°C]	SoC _{max} [%]	SoC _{min} [%]	EV _{ratio} [%]	P _{CH} [W]	Profile
I	Replicate	30	90	30	60	136	1
II	Low SoC	40	95	5	90	170	1
III	Different Profile	40	95	20	80	200	2
IV	Non-constant	40/20/30	85/85/90	20/20/15	80/40/20	72/200/136	1/1/1
V	Incl. Cal Storage	30/10/20	50/90/85	50/15/10	0/60/80	0/136/72	-1/1

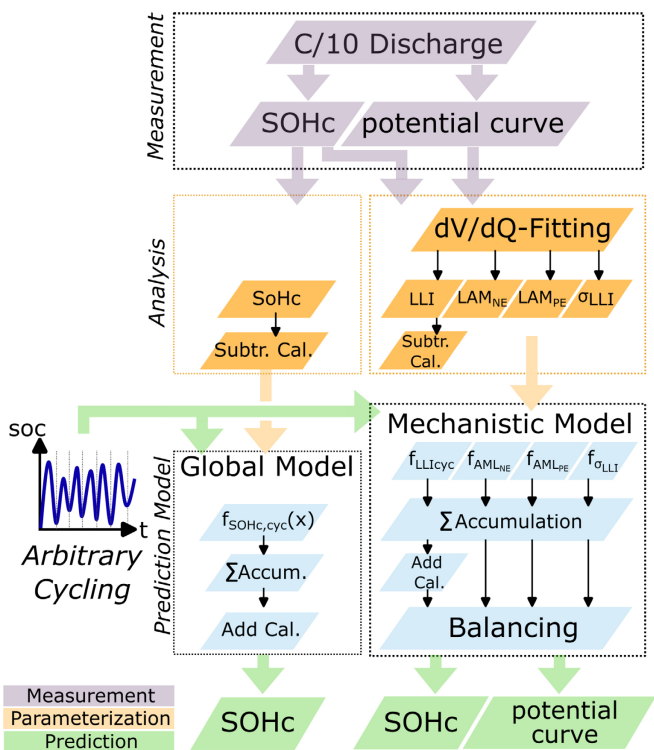


Figure 1. Scheme of the parameterization workflow of the global SoHC and the mechanistic model.

establish a mechanistic degradation prediction model that relies on the empirical component models to predict the SoHC and the discharge potential curve.

3.1. Calendar Aging Model

We partition the measured degradation into two components: a calendar component SoH_{cal} caused by storage at specific temperature and SoC conditions, and a cycle component SoH_{cyc} caused by the usage of the cell under load. This partitioning is commonly reported in literature, as calendar aging is typically time-dependent (t), while cycle aging is more dependent on the number of cycles, which is often expressed as energy or charge throughput (CTP).^[12,13]

The semi-empirical calendar aging model in Eq. (1) includes a temperature (T) dependency following the Arrhenius equation and a dependency on the open circuit voltage (OCV) motivated by the Tafel equation, which is commonly used in literature.^[14–16] The parameterization of the calendar model relies on additional tests and was introduced in our previous work.^[11] The parameters p are listed in Table S1.

$$SoH_{cal} = 100 + p_1 \exp\left(\frac{p_2}{T + 273}\right) \cdot \exp(p_3 OCV) \cdot t^{p_4} \quad (1)$$

3.2. Global Cycle Aging Model

Figure 2 shows all available degradation trajectories as well as single measurement points that we consider as outlier due to

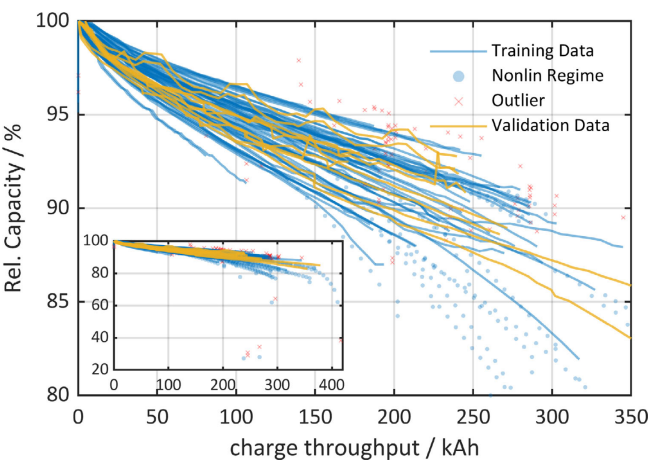


Figure 2. SoHC trajectories of all measured cells. Lines indicate the measurements we use for model parameterization. Outliers and measurements we attribute to the nonlinear regime are not considered in our model approach.

their distance from the original trajectories (red crosses). On top, we exclude points that are already in the nonlinear regime (dotted), as they would lead to an ill-conditioning of our model, which we discuss later on. An extensive analysis on this nonlinear trajectories including experimental post-mortem analysis can be found in Ref. [10].

In line with literature we assume that calendar and cycle aging are additive as expressed in Eq. (2), which allows us to subtract the estimated calendar degradation from the measured degradation SoH_{meas} .^[13,17]

$$SoH_{cyc} = SoH_{meas} - (100 - SoH_{cal}) \quad (2)$$

Therefore, we use a damage accumulation approach to estimate the calendar aging from temperature and SoC between the RPTs.

We use the base Eq. (3) to describe the cycle aging trajectory with the two parameters α and γ .

$$SoH_{cyc} = 100 + \alpha(x) \cdot CTP^\gamma \quad (3)$$

The parameter α represents the aging rate and is dependent on the aging conditions T , SoC_{max} , SoC_{min} , electric vehicle ratio (EV_{ratio}), and charging power (P_{CH}), which we collectively refer to as the predictor x .

The parameter γ controls the degree of passivation. While a $\gamma = 0.5$ is often found in literature as it was early derived from SEI-formation kinetics in calendar aging,^[18] this generalized power-law exponent is nowadays discussed both from theoretical and predictive performance side.^[19–21] Hence, we globally optimize γ on our dataset.

Eq. (3) restricts us to describe continuous aging trajectories without a knee, which is why we exclude the measurements of the aging trajectories that fall into the nonlinear regime.

A second order polynomial then describes the dependencies of α on the predictor values x_i and is fitted via linear regression.

Mdl Name	γ
Glob. SoH _C	0.65
LLI _{cyc}	0.79
LAM _{NE}	0.36
LAM _{PE}	0.83
σ_{LLI}	0.13

$$\alpha(x_i) = \beta_0 + \sum_i \beta_i x_i + \sum_i \beta_{ii} x_i^2 + \sum_i \sum_{j,j>i} \beta_{ij} x_i x_j \quad (4)$$

In contrast to the theory of design of experiments, which uses linear regression to describe the dependence of single-valued scalar response on the predictor, our response to every predictor is an entire SoH_C trajectory. Hence, we use a bi-level optimization approach to simultaneously optimize the passivation factor γ as well as the model coefficients β_i .^[21] By solving Eq. (3) for α , we create an outer loop that optimizes γ and an inner loop that solves the full linear model of α . Therefore, γ can be understood as part of a data transformation that linearizes the SoH_C trajectories into the domain of α (Eq. 5).

$$\alpha(x) = (\text{SoH}_{C,\text{cyc}} - 100) CTP^{-\gamma} \quad (5)$$

The inner loop minimizes the residual between the predicted and measured α values, which were transformed from SoH_C using the optimization function lsqcurvefit provided by MATLAB.

After optimizing γ , we use a step-wise backward elimination algorithm to retain only the statistically significant model terms β_i . A comparison of the estimated values of γ of the different models is listed in Table 2.

3.3. Mechanistic Model and dU/dQ -Fitting

In contrast to the global model approach, which directly uses SoH_C as the response, the mechanistic model approach expresses capacity degradation as a result of separate degradation modes that can be attributed to the cell's components. In the mechanistic model, the individual capacities and potential curves of the positive and negative electrodes, as well as their balancing, define the capacity that is theoretically available in the full cell between the lower and upper cutoff voltage in equilibrium conditions.^[3] Therefore, the degradation of the component capacities, LAM_{NE}, LAM_{PE} and LLI, describe the degradation of the full cell. This formulation of degradation provides more insight into the internal states of the cell and can help identify the most relevant aging mechanisms in the cell under certain aging conditions.

This section describes the process of finding the initial balancing and identifying the components' degradation from measured C/10 discharge potential curves. Subsequently, we will use these component trajectories to establish a mechanistic degradation prediction model that relies on empirical component models.

3.4. Reference Balancing

To determine the internal states of the mechanistic model at begin of life, we go through the following steps:

First, we measured negative and positive electrode potential curves by cycling harvested materials against Li/Li⁺ in experimental coin-sized cells. We take the physical relationship between the electrodes voltage U_{NE} and U_{PE} and their lithiation degree χ_{NE} and χ_{PE} from literature.^[22,23]

The full cells potential U_{fc} results from the difference between U_{PE} and U_{NE} in their corresponding range of lithiation χ_i [0,1] (Eq. 6).

$$U_{fc} = U_{\text{PE}}(\chi_{\text{PE}}) - U_{\text{NE}}(\chi_{\text{NE}}) \quad (6)$$

Hence, we need to determine the four parameters $\chi_{\text{NE},0}$, $\chi_{\text{PE},0}$, $\chi_{\text{NE},100}$, $\chi_{\text{PE},100}$ which define the respective electrodes lithiation degree at 0 % and 100 % SoC and dictate the balancing of the electrodes.

We use the iterative multi-step fitting algorithm described by Fath et al. that optimizes these four parameters in a windowed approach. It mainly minimizes the error between fitted and measured BOL dU/dQ curve on pouch cell level, but also considers the error of the respective dQ/dU curve.^[24,25]

We take the potential curve of a C/10 discharge on full cell level for parameterization. The low C-rate attenuates overpotentials, however for future work measuring and averaging both charge and discharge curves would allow to work with a more accurate quasi-open circuit voltage (quasi-OCV).

As a result from this fitting algorithm, the electrodes theoretical total capacities $Q_{i,\text{tot}}$, which is the charge over the entire range of lithiation can then be calculated from the measured full cell capacity Q_{fc} with Eq. 7.

$$Q_{i,\text{tot}} = \frac{Q_{fc}}{|\chi_{i,0} - \chi_{i,100}|} \quad (7)$$

We will refer to this set of parameters derived from the BOL measurements as reference balancing. Figure 3c shows the reconstructed dU/dQ curve (blue) from the mechanistic model versus the measured curve (black). Obviously, the four parameters $\chi_{i,\text{soc}}$ that define the reference balancing are not sufficient to accurately reconstruct the dU/dQ curve. In the next section, we will discuss what is lacking in the reference balancing to achieve a good fit.

3.5. Aged Balancing

By definition, the determined reference balancing does not contain any component losses. Hence, LLI, LAM_{NE}, LAM_{PE} and σ_{LLI} can describe the changes of the internal states due to aging relative to the reference balancing.

LAM_{NE} and LAM_{PE} define the loss of electrode capacity $Q_{i,\text{tot},\text{deg}}$ relative to their reference state $Q_{i,\text{tot},\text{ref}}$ due to a decrease of accessible intercalation sites.

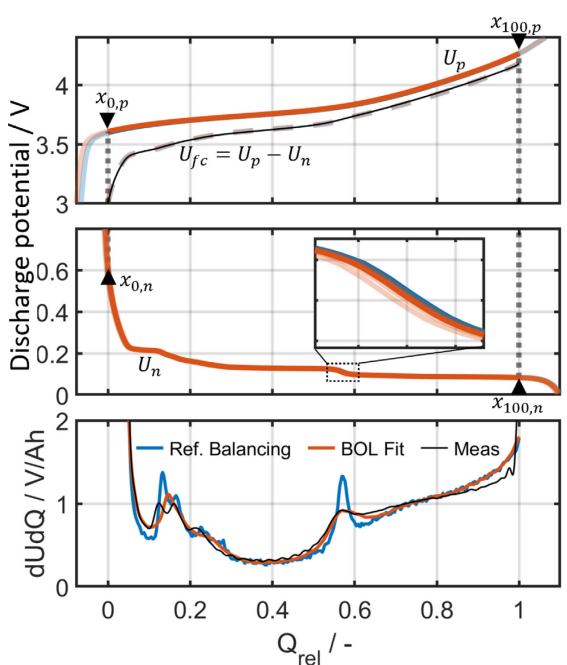


Figure 3. a) Balanced positive electrode potential curve with indicated lithiation degree at 0 % and 100 % SoC and resulting full cell potential calculated from the electrode potentials (dotted) and measured (line). b) Balanced negative electrode potential curve and contribution of σ_{LLI} that describes the inhomogeneous distribution of LLI in the electrode as superposition segments in parallel connection with varying LLI. c) Comparison between measured dU/dQ , the recreated dU/dQ from initial balancing and the recreated dU/dQ from the BOL-Fit, respectively.

$$LAM_i = 1 - \frac{Q_{i,tot,deg}}{Q_{i,tot,ref}} \quad (8)$$

LLI defines the loss of cyclable lithium, which in turn leads to a slippage between the electrodes alignment.

The model relies on the conservation of the total lithium amount Li_{tot} , which results from the amount of Lithium initially stored in the positive and negative electrode at a given SoC of the fullcell (Eq. 9).

$$Li_{tot} = \chi_{0,NE} \cdot Q_{NE,tot} + \chi_{PE,0} \cdot Q_{PE,tot}. \quad (9)$$

LLI again describes the loss of total cyclable lithium amount relative to the reference state (Eq. 10).

$$LLI = 1 - \frac{Li_{tot,deg}}{Li_{tot,ref}} \quad (10)$$

As LAM and LLI result in changing electrode capacities and slippage between the electrode potentials, we need to determine the new lithiation range on both electrodes that defines the full cell potential between 0 % and 100 % SoC. For that we interpolate the electrode potential curves based on their capacity and match the points where the negative electrode is fully delithiated, and the entire lithium is found on the positive electrode,

$$\chi_{NE} = 0 \quad (11)$$

and

$$\chi_{PE} = \frac{Li_{tot} \cdot (1 - LLI)}{Q_{PE,tot,ref} \cdot (1 - LAM_{PE})}. \quad (12)$$

Likewise we match the curves at the charged end by attributing the entire lithium to the negative electrode:

$$\chi_{PE} = 0 \quad (13)$$

and

$$\chi_{NE} = \frac{Li_{tot} \cdot (1 - LLI)}{Q_{NE,tot,ref} \cdot (1 - LAM_{NE})}. \quad (14)$$

This approach hypothetically overloads the negative electrode and results in lithiation degrees exceeding 1, which is physically not possible. Still, this step allows to balance the electrodes new capacity with the available lithium at the hypothetical endpoints and thereby matches each χ_{NE} to a corresponding χ_{PE} . With this matching, we can interpolate again to find the lower and upper cutoff voltages on the resulting full cell potential and thus the new electrodes lithiation degrees $\chi_{NE,0}$, $\chi_{PE,0}$, $\chi_{NE,100}$, $\chi_{PE,100}$ at 0 % and 100 % SoC.

In line with the discussion of Dubarry et al., our approach of basing the mechanistic model on the lithiation degree does not distinguish between LLI caused by SEI-formation, plating or even loss of lithiated active material.^[26] This means that every LAM_{PE} will also lead to LLI, as the active material still has a certain lithiation degree at 100 % SoC. Our approach of tracking the conservation of total lithium automatically ensures every LLI is properly accounted, no matter of what origin.

Additionally, σ_{LLI} describes the degree of inhomogeneity of LLI within the cell that can be observed as flattening of the dU/dQ peaks.^[27–29] This inhomogeneity has been reproduced by describing the cell as segments with variable LLI that are electrically connected in parallel.^[24,25] We assume a linear distribution of LLI, where σ_{LLI} defines the min and max values via $LLI \pm \frac{\sigma_{LLI}}{2}$. The inverse weighted sum of the segments inverse $(dU/dQ)^{-1}$ then gives the final dU/dQ of the full cell, which also describes the discharge potential curve.

With the definitions from above the four parameters LLI, LAM_{NE} , LAM_{PE} and σ_{LLI} can adjust the reference balancing to fit any aged balancing. The iterative fitting approach presented by Fath et al.^[24] uses these aging modes to minimize the error between measured and reconstructed dU/dQ .

First, we will use the algorithm on the BOL measurements to examine why the reference balancing does not perfectly match the measured dU/dQ . Figure 3 presents the reference balancing in blue and one example of a recreated BOL discharge potential as result of the fitting procedure in orange. Clearly, LLI is not equally distributed in our cells at BOL, as using the fitting algorithm based on the reference balancing on the BOL measurements leads to a $\sigma_{LLI} > 0$. In previous work, we have already observed that LLI is not homogeneously distributed at BOL. It homogenizes in the beginning of the test and becomes less homogeneous afterward.^[10] We will discuss the implications of this behavior on our prediction model later.

Using the fitting algorithm on the measured BOL curve also returns non-zero values for LAM_{PE} and LAM_{NE} . The example in

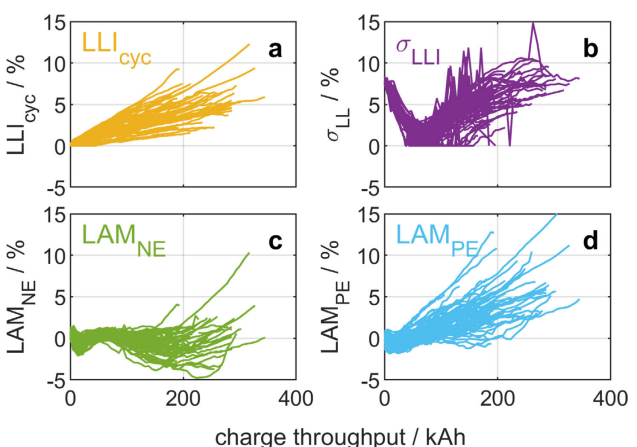


Figure 4. Component Losses estimated from the dU/dQ -fitting algorithm. a) shows LLI_{cyc} where calendar aging was already subtracted, whereas b-d) show the Losses as fitted.

Figure 3 even shows slightly negative LAM_{PE} , which is indicated by the orange positive electrode potential curve being slightly longer on the discharged side.

Next, we use the algorithm to determine the component losses throughout the aging experiment, which are presented in Figure 4. Again, we exclude measurements that are in the nonlinear regime, as our post-mortem analysis has already shown that the aging trajectories also enter a nonlinear regime on the component level.^[10]

Based on the reference balancing, the 60 cells in the aging matrix all show slightly different initial losses at BOL, as seen in Figure 4. Similar to σ_{LLI} , we observe a general trend of LAM_{NE} and LAM_{PE} first dropping even below zero and then rising again. It is not entirely clear where this initial behavior comes from. It might even be an artifact of the fitting process because estimating LAM_{PE} is difficult in a low-nickel positive electrode, as the positive electrodes potential doesn't lead to distinctive features in the dU/dQ curve. For future work, putting more focus on the incremental capacity (dQ/dU) in the fitting as described by Dubarry et al.^[30] might help to fit LAM_{PE} more accurately and alleviate this offset.

3.6. Component Models

Now that we have determined the trajectories of the component losses over aging for all 60 cells, we parameterize a prediction model for each component.

To simplify, we use the same base equation for each component model as we introduced for the global SoH_C model in section "Global Cycle Aging Model". Keep in mind that a more physically informed or empirically suitable equation for the different component models might improve model accuracy and generalizability.

Separating cycle aging from calendar aging is more difficult in the mechanistic model, as the calendar aging could contribute to each of the component losses. Unfortunately we do not have a dataset that would let us use the dU/dQ -fitting to parameterize a mechanistic model for calendar aging as well. But as our previous

post-mortem analysis of the cells has detected only LLI in the calendar aged cells,^[10] we attribute the entire capacity loss which the semi-empirical calendar aging model predicts, to LLI_{cal} .

$$LLI_{tot} = LLI_{cyc} + LLI_{cal} \quad (15)$$

As we have no estimate of LLI_{cal} , we use the mechanistic framework to iteratively minimize Eq. (2) by varying LLI_{cyc} , where $SoH_{cyc,mdl}(LLI_{cyc})$ corresponds to the predicted SoH_C from the mechanistic model when varying (LLI_{cyc}) . Thereby, we determine the amount of LLI_{cyc} that corresponds to the $SoH_{cyc,meas}$.

$$\Delta SoH_C = SoH_{cyc,mdl}(LLI_{cyc}) - SoH_{cyc,meas} \quad (16)$$

As the inhomogeneity is also not driven by calendar aging,^[10] we attribute the full development of inhomogeneity to cycle aging. This results in LLI_{cyc} that describes the capacity loss that we expect when adjusting the measured capacity with the empirical calendar aging model.

We are aware, that this workaround is not optimal, but show that our hybrid mechanistic model approach can also be used with incomplete data if there are additional analysis results that allow for a cautious simplification of the calendar and cycle aging approach. Still, we would highly recommend to ensure a complete calendar aging parameterization data set for various aging conditions as well.

With the component losses LLI_{cyc} , LAM_{PE} , LAM_{NE} and σ_{LLI} that correspond to pure cycle aging, the model parameterization is straightforward and follows the routine described in section "Global Cycle Aging Model". Table 2 shows the estimated exponent γ for the different component models.

There is one additional step in the component model of LAM_{PE} . LAM_{PE} dropping significantly below zero in the beginning greatly disturbs the fitting, where we dictate an aging trajectory starting at 0 with a strictly monotonic behavior. Thus, a transforming the estimated LAM_{PE} values reduces the residuals and the bias in the component model. We determine the mean of the minimally estimated LAM_{PE} of each cell, which is 0.786 %, and subtract it from the LAM_{PE} trajectories, hence shifting LAM_{PE} towards positive values. This global offset has to be added to every predicted LAM_{PE} again before using it in the mechanistic model. This data transformation is likely not necessary for other cell-types, if the cell does not show the initial effect of decreasing homogeneity and decreasing LAM_{PE} . While LAM_{NE} shows an even stronger drop below zero in the beginning, adding an offset does not improve the prediction model, as the residuals do not show a strong systematic trend.

Figure 5 shows the residuals on the parameterization data for each component model. As expected, the model approach becomes less suitable with increasing complexity of the trajectories. While the model for LLI shows similarly low residuals with an overall RMSE of 0.44 as the global SoH_C model. Surprisingly, the exponent $\gamma = 0.79$ defines a more linear trajectory for the LLI component model than we found for the global SoH_C model ($\gamma = 0.65$). The models for LAM_{NE} or LAM_{PE} exhibit larger deviations with an RMSE of 1.01 and 0.81.

The systematic trend in the residuals of the σ_{LLI} model shows that our model approach cannot accurately predict the more

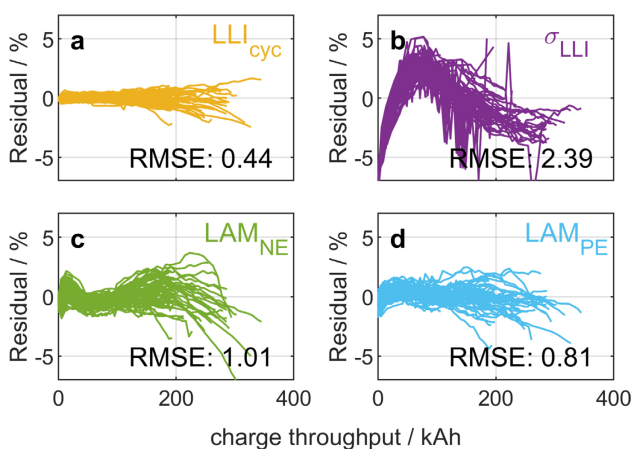


Figure 5. Residuals between measured and predicted component losses and the overall RMSE of each component model based on parameterization data.

complex U-shape trajectory. Nevertheless, we choose to not further optimize the model approach for σ_{LLI} and examine its influence on the model performance in section “Prediction of Discharge Potential”.

3.7. Model Predictions

So far, with the component models as well as the global SoH_C model we can predict a continuous degradation trajectory based on a constant predictor x over a continuous charge throughput.

However, aging conditions vary over time in a realistic usage. Therefore, we will now describe how to accumulate the degradation that the cell suffers from cycles with varying aging conditions.

We use an SoH_C based damage accumulation, which is a common approach in literature for both calendar and cycle aging.^[13,14,31,32]

Recently, Karger et al. have theoretically and experimentally compared the CTP based and the SoH_C based accumulation method, where the latter has turned out to be more accurate.^[33]

We segment time-series data into single cycles that are defined between two charging events with a minimum of $\Delta SoC > 10\%$ to exclude smaller recuperation charging. In every cycle we evaluate the predictor values T , SoC_{max} , SoC_{min} , EV_{ratio} , P_{CH} and CTP as input for the cycle aging models as well as the duration at different temperatures and SoCs as input for the calendar aging model.

The SoH_C based damage accumulation approach assumes history independence, which means that the damage caused by an arbitrary cycle is only dependent on the predictor and the SoH_C at beginning of the cycle, but not on the aging conditions that have lead to this degradation.

In practice, the SoH_C at beginning of the cycle is converted to an equivalent charge throughput CTP_{eq} that would lead to the same degradation under the aging conditions of that cycle.

$$CTP_{eq} = \left(\frac{SoH_{n-1} - 100}{\alpha_n(x_n)} \right)^{\frac{1}{\gamma}} \quad (17)$$

Then, the SOH_{cyc} after the n -th cycle is calculated with Eq. (18) using the sum of the equivalent CTP and the CTP of the cycle.

$$SOH_{cyc} = 100 + \alpha_n \cdot (CTP_{eq} + CTP_n)^{\gamma} \quad (18)$$

We treat each component model separately.

The mechanistic model then determines the aged balancing from all four predicted component losses. This in turn defines the dischargeable capacity Q_{fc} between upper and lower voltage boundary and thus the SoH_{cyc} as described in section Mechanistic Model and dU/dQ -Fitting.

To predict the combined SoH_C from cycle and calendar aging, we sum them up in the end over the entire trajectory, as this is closest to how we subtracted the calendar aging in the beginning and thus corresponds to how the models were parameterized. In case of the mechanistic model, this means again to use Eq. (16) to find the LLI that best matches the accumulated capacity loss from cycle and calendar aging.

4. Results and Validation

After having explained the model structure and parameterization in detail, we will now compare and discuss the models performance first on their parameterization data and then on independent validation test cases.

4.1. Comparison on Parameterization Data

Similar to the parameterization we use only one mean predictor to describe the constant aging conditions throughout each test to calculate the degradation rates from the regression models and predict the trajectory. **Figure 6** shows the residuals between the measured and predicted SoH_C of both the global SoH_C model and the mechanistic model.

Measurements that fall into the nonlinear regime are indicated as dots, but are not included in the RMSE calculation, as we are aware that the model is only valid until the start of the nonlinear regime.

Both models perform very similar on the parameterization data, with the global SoH_C model exhibiting a slightly better overall RMSE of 0.42 compared to the RMSE of 0.62 of the mechanistic model. Additionally, both models show very comparable behavior with respect to the aging conditions. In both figures, the colors highlight the aging curves at the same aging conditions. Remarkably, both models seem to have similar aging conditions marking the lower and upper boundary of the residual distribution. Therefore, the slightly worse accuracy of the mechanistic model is not surprising, given the additional steps that introduce uncertainty from dU/dQ fitting over balancing to capacity calculation.

4.2. Comparison on Additional Validation Data

We now gradually increase the difficulty by comparing the model predictions to independently measured validation tests.

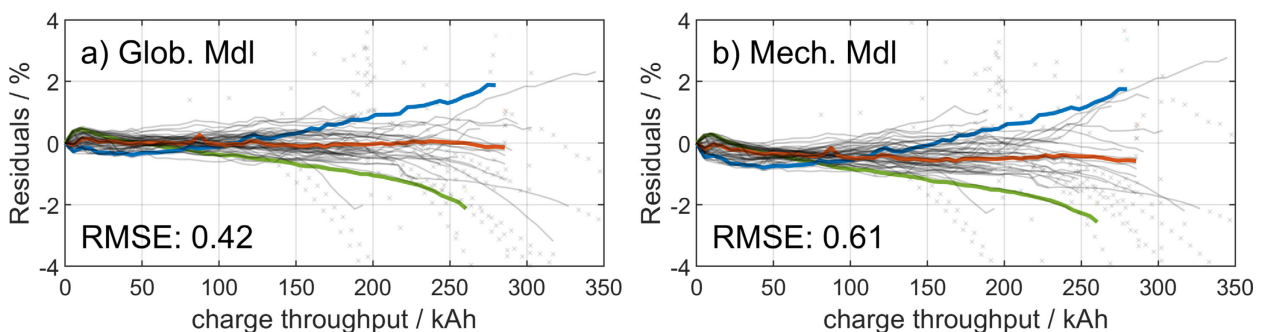


Figure 6. Comparison between the predictive performance of a) the global SoH_c model and b) the hybrid mechanistic model on parameterization data. Dotted measurement points indicate aging in the nonlinear regime that are not considered in the calculation of RMSE. Colors highlight the same aging conditions in both cases, showing the divergence of aging prediction in the extreme cases.

For this part of the validation, we also switch to the prediction methodology of SoH_c based damage accumulation as described in section “Model Predictions”.

I The first validation experiment reproduces the center point of the original aging test to show the comparability of the tests. Figure S1 compares the degradation trajectories of parameterization and validation experiment. It shows, that the validation experiment exhibits slightly higher degradation. This can explain why both SoH_c model and the mechanistic model tend to underestimate the measured degradation.

II The second validation experiment in Figure 7b tests the extrapolation performance by discharging to a SoC_{\min} of 5 %, which is lower than the lowest tested SoC_{\min} in the aging experiment at 21 %. With an RMSE of 1.0 for the global SoH_c model and 1.4 for the mechanistic model, both models show their worst performance on this test. This emphasizes that empirical models should not be used to extrapolate, as they do not base on any physical relationship. This is in line with our previous work, where SoC_{\min} showed a second-order dependency with increasing degradation towards low values,^[11] and would thus also overestimate the degradation when extrapolating.

III The third validation experiment, Figure 7c, uses a different power profile for discharging and hence tests the generalizability of our method to estimate the cycle load on the cell and correlate it to a certain amount of degradation. The difference between the power profiles, however, is not exaggerated and shown in more detail in the Supporting Information S3. In this case, both models show good performance. While the mechanistic model predicts a slightly more linear trajectory, it again underestimates the aging.

IV In the fourth validation experiment, Figure 7d, the aging conditions change after every three cycling sequences, which results in the wavy trajectory. While the measurements show a periodical gain in capacity, which we attribute to the reversible capacity effect,^[34,35] our models can only describe a monotonically decreasing SoH_c by design. Still, both models predict a trajectory that follows the measurement with low deviation (RMSE Glob.Mdl. 0.3 and Mech.Mdl. 0.5). Here again, the mechanistic model tends to underestimate the degradation without diverging from it. Overall, the damage accumulation approach leads to a realistic prediction in our validation test cases.

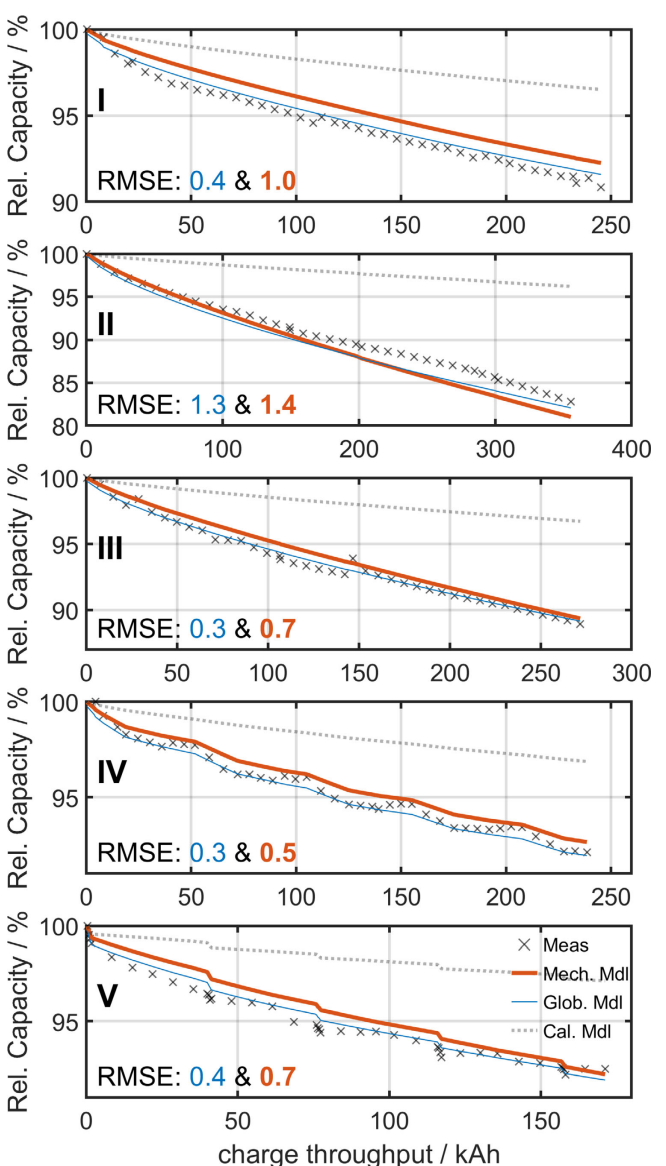


Figure 7. Measured SoH_c trajectory of one cell each of the five different validation tests I–V and predictions from the previously parameterized global SoH_c and mechanistic aging model. The contribution of calendar aging is indicated as dotted line. Mind the different scaling of x- and y-axes.

V The last validation experiment in Figure 7e again switches aging conditions after every three RPTs and even includes a pure calendar aging sequence. This is reflected as sudden drops in the degradation trajectory, as the charge throughput does not progress in the calendar sequence but the degradation does. Here again, both models reproduce these capacity drops in the trajectory. Both models seem to be more linear than the measured trajectory, and while they underestimate the degradation in the first half, they cross the aging trajectory at around 150 kAh and likely overestimate the aging afterwards. Nonetheless, with an RMSE of 0.4 and 0.7, respectively, both models predict the measured aging well.

The dotted line shows the contribution of calendar aging in every test case. Even in the accelerated aging test that was set up to validate cycle aging, we attribute up to a third of the total degradation to calendar aging. Even though we focus on how to accurately predict cycle aging in this work, we also want to stress that calendar aging also has a huge, if not the biggest impact on predictions over the entire battery lifetime.

Overall, the global SoH_C model is more accurate in predicting the capacity trajectory. Given the increased complexity and additional steps in the mechanistic model that introduce uncertainty, this was expected. Also, the mechanistic model seems to adapt a degradation trajectory that is a little too linear in all validation tests, which is caused by the greater estimated value of γ in comparison to the global SoH_C model.

We have seen from previous analyses that the capacity degradation in this cell-type is dominated by LLI only. Therefore, the model comparison comes down to a one to one comparison between the global model and the LLI component model, where we cannot expect any benefit from the component model, as we are using the same base equation. This also explains why both models show very similar residuals on comparable aging conditions and also when entering the nonlinear regime.

However, the mechanistic model can still hold advantages over the global SoH_C approach. It could outperform the global SoH_C model in case LAM_{PE} becomes dominating, as shown by

Karger et al.^[8] In that case, the mechanistic model could describe a kneepoint in the SoH_C trajectory even with continuous component models. Additionally, the mechanistic model challenges how we think about path-dependency.^[33,36,37] While the global SoH_C model as well as the component model are history- and path-independent through their mathematical commutativity,^[33] the mechanistic model introduces a history-dependency on SoH_C level. A certain SoH_C can be the result of multiple combinations of component losses, and thus the degradation of the next step is no longer only dependent on the governing SoH_C. While this is a theoretical perspective, this effect should be examined more thoroughly when discussing path-dependence. Furthermore, the mechanistic model can describe more than just capacity, which we discuss in the next section.

4.3. Prediction of Discharge Potential

Analyzing changes of the OCV curve through degradation is the foundation of the mechanistic model. While these changes help us to better understand aging, they can also have a negative impact e.g. on the accuracy of SoC estimation in a battery management system. By predicting the balancing between the electrodes, we can leverage the mechanistic model to predict these changes of the OCV due to calendar and cycle aging over the lifetime of the battery.^[7,8]

In this section we discuss the models capabilities to predict discharge potential curves based on the previously introduced validation tests.

Figure 8 shows the validation tests I–V in the columns. The upper row compares the development of the RMSE between measured and predicted discharge potential curve with the RMSE between measurement and the recreated discharge potential curves via dU/dQ -fitting over lifetime. The RMSE of predictions shows two model variants where we consider or neglect σ_{LLI} , which we discuss later. The middle and bottom rows compare the the predicted component losses (line) with the corresponding

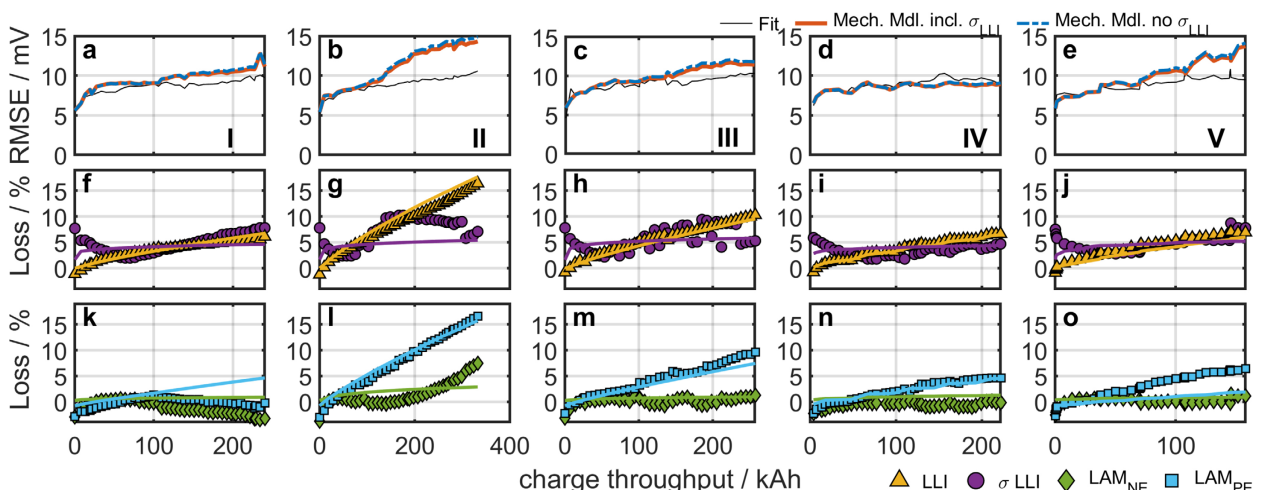


Figure 8. Different validation tests (columns). The Upper row (a–e) compares the RMSE of the predicted discharge potential curve at each RPT when considering (blue) or neglecting (orange) σ_{LLI} with the discharge potential directly recreated from the dU/dQ -fit. The middle and bottom rows show the estimated Losses from the dU/dQ -fitting (marker) as well as the predicted Losses from the component models (lines). Mind the different scaling of the x-axis.

estimates from the dU/dQ -fitting algorithm (marker). Measurements of the discharge potential curve were evaluated in the voltage window between 3.0 V and 4.18 V. The mechanistic model predicts the discharge potential curve in the same range.

Besides test case 2, which tests the extrapolation to low SoC_{min}, the RMSE of the predictions hardly deviates from the recreated potential curve through dU/dQ -fitting (grey) in Figure 8a–e. The mechanistic model can thus track the degraded potential curve as closely as possible. Being better than the recreation through dU/dQ -fitting would also mean being better than the method that has been used to supply the parameterization data for the component models.

Still, the question arises, where the error that we even observe in the directly recreated potential curve has its origin.

The residuals of the predicted potential curve in Figure 9b–d reveal that the main fraction of the error comes from the region between 60 % and 100 % SoC. The dU/dQ comparison between the measured and predicted curve at EOL clearly shows that the

actual measured potential curve exhibits a smaller gradient in that region than the predictions. We observed this effect already in the BOL reference fit in Figure 3c.

Most likely, this error results from an inaccurate fit of LAM_{PE} based on the dU/dQ curves. As described before, estimating LAM_{PE} on low-nickel positive electrodes with the dU/dQ -fitting is less accurate as there are no distinct features that allow an accurate tracking of LAM_{PE}.

With a better matching reference balancing, which is more easily achieved with nickel-rich materials that exhibit distinctive features in the dU/dQ curve, we expect this error to be drastically reduced.

Lastly, we discuss the influence of inhomogeneity, which is described by σ_{LLI} . Due to the σ_{LLI} model containing systematic trends in the residual, we examine the effect of entirely neglecting σ_{LLI} in the prediction.

In Figure 8a–e, the orange line shows the RMSE of the predictions when considering σ_{LLI} , whereas the blue line presents the RMSE without considering σ_{LLI} . Both predictions align almost perfectly, meaning the influence of σ_{LLI} is negligible in comparison to the influence of the other losses. This is surprising at first, given the contribution of σ_{LLI} to a better fit in the dU/dQ curve. Figure 9a shows the previously discussed effect of peak flattening and broadening through inhomogeneity, where σ_{LLI} is vital to reduce fitting error.

The reason becomes apparent when looking at the residuals of the prediction over the entire SoC range in Figure 9b–d. While the potential curve described with σ_{LLI} in Figure 9b and 9c show a smooth error around the peak at 60 % SoC, Figure 9d has a local s-shaped error, which corresponds to predicting this peak too sharply. This shows that σ_{LLI} does have the expected effect of increasing the accuracy of the predicted potential curve around 60 % SoC, but it is a very local effect and minor in comparison to the overall error.

5. Conclusions

In this study, we have compared the performance of a global SoH_C model and a hybrid mechanistic model approach in predicting the degradation behavior of lithium-ion batteries. Our results show that overall, the global SoH_C matches both the passivating behavior as well as the absolute values of the SoH_C degradation better than the hybrid mechanistic model.

However, we can only draw this conclusion in the boundaries of the investigated cell and its degradation behavior where LLI dominates the SoH_C degradation. While the global SoH_C model proves to be a very good and easy approach if the focus lies on capacity degradation, we also acknowledge that the mechanistic model adds a more physically informed layer and can thus provide a more comprehensive insight into the degradation. This already pays off in the parameterization stage, where the mechanistic model enforces a more thorough analysis of the aging tests. Additionally, other works could point out that the mechanistic model is able to cover knee-points in the SoH_C trajectory, i.e. when LAM_{PE} has outpaced LLI over time and has thus induced a kink in the SoH_C trajectory.

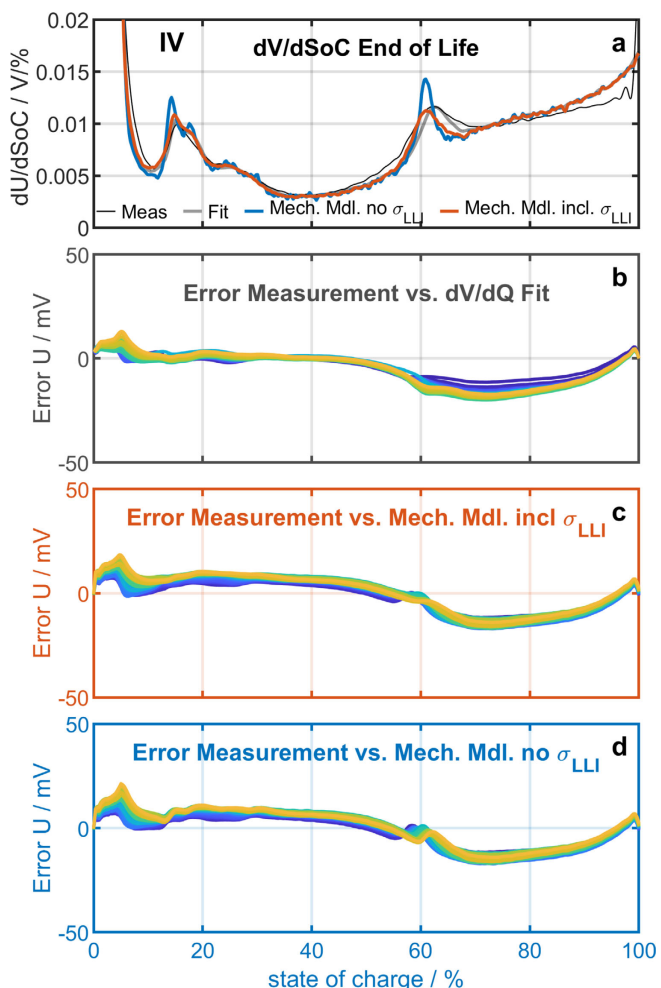


Figure 9. a) Comparison of measured, fitted and predicted dU/dQ curve on validation TestCase IV. b–d) Residual of measured potential curve vs b) recreated potential curve from dU/dQ -fit, c) predicted potential curve when considering σ_{LLI} and d) predicted potential curve without considering σ_{LLI} . Colors of the heading reflect the color of EOL $dU/dSoC$ in a). Colors from blue to yellow indicate progressing charge throughput. For a colored version, we refer to the web-version of the article.

The most significant advantage of the mechanistic model approach, however, is its ability to not only predict SoH_C, but also changes of the potential curve, which could easily be applied to quasi-OCV or OCV curves. Here we found the largest error being rooted in the deviating initial reference balancing. Investigating the impact of inhomogeneous LLI, we have found that while σ_{LLI} helps to fit and assign changes in dU/dQ curves to the component losses, it does not contribute significantly to a more accurate prediction of aged potential curves.

In short, the advantages of the mechanistic model approach are:

- Enabling potential-curve prediction
- More insight into root causes of aging
- Model LAM_{PE}-induced knee

Whereas the advantages of the global SoH_C model are:

- Easy analysis and parameterization
- Accurate prediction of SoH_C in linear regime

Furthermore, we have shown that calendar aging is responsible for a significant amount of the total degradation, even on short time-spans. While cycle aging is often more in focus due to its more complex nature of modeling, we like to point out that accurately predicting calendar aging is very important, especially when predicting a battery lifetime over 10–15 years.

Overall, the mechanistic model approach has more potential to grow in our view. Further research could work on using physically motivated models for component degradation, as we previously discussed in Ref. [38]. Introducing a coupling between the component models, as it is often discussed for physical models of individual aging mechanisms,^[1] could also be promising. Finally, determining model equations that better fit the underlying form of the trajectory, e. g. via ML methods,^[39,40] could improve the models predictive performance.

Acknowledgments

We thankfully acknowledge the Mercedes-Benz AG for funding of the extensive cyclic aging tests.

Conflict of Interests

The authors declare no conflict of interest.

Data Availability Statement

Research data are intellectual property of the Mercedes-Benz AG and cannot be shared.

Keywords: lithium ion battery · battery aging · lifetime prediction · mechanistic model · design of experiment · OCV prediction

- [1] S. E. J. O’Kane, W. Ai, G. Madabattula, D. Alonso-Alvarez, R. Timms, V. Sulzer, J. S. Edge, B. Wu, G. J. Offer, M. Marinescu, *Phys. Chem. Chem. Phys.* **2022**, *24*, 7909.
- [2] F. Brosa Planella, W. Ai, A. M. Boyce, A. Ghosh, I. Korotkin, S. Sahu, V. Sulzer, R. Timms, T. G. Tranter, M. Zyskin, S. J. Cooper, J. S. Edge, J. M. Foster, M. Marinescu, B. Wu, G. Richardson, *Prog. Energy* **2022**, *4*, 042003.
- [3] M. Dubarry, C. Truchot, B. Y. Liaw, *J. Power Sources* **2012**, *219*, 204.
- [4] I. Bloom, J. Christopheresen, K. Gering, *J. Power Sources* **2005**, *139*, 304.
- [5] P. M. Attia, A. Bills, F. Brosa Planella, P. Dechent, G. dos Reis, M. Dubarry, P. Gasper, R. Gilchrist, S. Greenbank, D. Howey, O. Liu, E. Khoo, Y. Preger, A. Soni, S. Sripad, A. G. Stefanopoulou, V. Sulzer, *J. Electrochem. Soc.* **2022**, *169*, 060517.
- [6] M. Dubarry, D. Beck, *Accounts Mater. Res.* **2022**, *3*, 843.
- [7] A. Karger, J. Schmitt, C. Kirst, J. P. Singer, L. Wildfeuer, A. Jossen, *J. Power Sources* **2023**, *578*, 233208.
- [8] A. Karger, J. Schmitt, C. Kirst, J. P. Singer, L. Wildfeuer, A. Jossen, *J. Power Sources* **2024**, *593*, 233947.
- [9] J. Stadler, C. Krupp, M. Ecker, J. Bandlow, B. Spier, A. Latz, *J. Power Sources* **2022**, *521*, 230952.
- [10] J. Stadler, T. K. Groch, M. García, M. Storch, J. Fath, M. Ecker, A. Latz, *J. Energy Storage* **2023**, *65*, 107247.
- [11] J. Stadler, C. Krupp, M. Ecker, J. Bandlow, B. Spier, A. Latz, *J. Power Sources* **2022**, *521*, 230952.
- [12] S. Ganterbein, M. Schönleber, M. Weiss, E. Ivers-Tiffée, *Sustainability* **2019**, *11*, 6697.
- [13] E. Sarasketa-Zabala, E. Martínez-Laserna, M. Berecibar, I. Gandiaga, L. M. Rodríguez-Martínez, I. Villarreal, *Appl. Energy* **2016**, *162*, 839.
- [14] S. L. Hahn, M. Storch, R. Swaminathan, B. Obry, J. Bandlow, K. P. Birke, *J. Power Sources* **2018**, *400*, 402.
- [15] E. Sarasketa-Zabala, I. Gandiaga, L. M. Rodríguez-Martínez, I. Villarreal, *J. Power Sources* **2014**, *272*, 45.
- [16] M. Ecker, J. B. Gerschler, J. Vogel, S. Käbitz, F. Hust, P. Dechent, D. U. Sauer, *J. Power Sources* **2012**, *215*, 248.
- [17] T. Gewald, A. Candussio, L. Wildfeuer, D. Lehmkuhl, A. Hahn, M. Lienkamp, *Batteries* **2020**, *6*, 6.
- [18] H. J. Ploehn, P. Ramadass, R. E. White, *J. Electrochem. Soc.* **2004**, *151*, 456.
- [19] P. M. Attia, W. C. Chueh, S. J. Harris, *J. Electrochem. Soc.* **2020**, *167*, 090535.
- [20] L. Kolzenberg, A. Latz, B. Horstmann, *ChemSusChem* **2020**, *13*, 3901.
- [21] P. Gasper, K. Gering, E. Dufek, K. Smith, *J. Electrochem. Soc.* **2021**, *168*, 020502.
- [22] J. Schmalstieg, *Physikalisch-elektrochemische Simulation von Lithium-Ionen-Batterien: Implementierung, Parametrierung und Anwendung*, volume Diss., **2017**.
- [23] J. Kasnatscheew, S. Röser, M. Börner, M. Winter, *ACS Appl. Energ. Mater.* **2019**, *2*, 7733.
- [24] J. P. Fath, D. Dragicevic, L. Bittel, A. Nuhic, J. Sieg, S. Hahn, L. Alsheimer, B. Spier, T. Wetzel, *J. Energy Storage* **2019**, *25*, 100813.
- [25] J. Sieg, M. Storch, J. Fath, A. Nuhic, J. Bandlow, B. Spier, D. U. Sauer, *J. Energy Storage* **2020**, *30*, 101582.
- [26] M. Dubarry, V. Agrawal, M. Hüské, M. Kuipers, *J. Electrochem. Soc.* **2023**, *170*, 070503.
- [27] M. Lewerenz, A. Marongiu, A. Warnecke, D. U. Sauer, *J. Power Sources* **2017**, *368*, 57.
- [28] M. Lewerenz, D. U. Sauer, *J. Energy Storage* **2018**, *18*, 421.
- [29] M. Lewerenz, G. Fuchs, L. Becker, D. U. Sauer, *J. Energy Storage* **2018**, *18*, 149.
- [30] M. Dubarry, D. Anseán, *Front. Energy Res.* **2022**, *10*, 1023555.
- [31] H. Wenzl, A. Haubrock, H.-P. Beck, *Zeitschrift für Phys. Chemie* **2013**, *227*, 57.
- [32] E. Sarasketa-Zabala, I. Gandiaga, E. Martínez-Laserna, L. M. Rodríguez-Martínez, I. Villarreal, *J. Power Sources* **2015**, *275*, 573.
- [33] A. Karger, L. Wildfeuer, D. Aygül, A. Maheshwari, J. P. Singer, A. Jossen, *J. Energy Storage* **2022**, *52*, 104718.
- [34] M. Lewerenz, J. Münnix, J. Schmalstieg, S. Käbitz, M. Knips, D. U. Sauer, *J. Power Sources* **2017**, *345*, 254.
- [35] M. Lewerenz, P. Dechent, D. U. Sauer, *J. Energy Storage* **2019**, *21*, 680.
- [36] T. Raj, A. A. Wang, C. W. Monroe, D. A. Howey, *Batteries & Supercaps* **2020**, *3*, 1377.
- [37] M. Rogge, A. Jossen, *Batteries & Supercaps* **2024**, *7*, e202300313.
- [38] L. Kolzenberg, J. Stadler, J. Fath, M. Ecker, B. Horstmann, A. Latz, *J. Power Sources* **2022**, *539*, 231560.
- [39] K. Schofer, F. Laufer, J. Stadler, S. Hahn, G. Gaiselmann, A. Latz, K. P. Birke, *Adv. Sci. (Weinheim, Baden-Württemberg, Germany)* **2022**.

[40] P. Gasper, N. Collath, H. C. Hesse, A. Jossen, K. Smith, *J. Electrochem. Soc.* 2022, 169, 080518.

Manuscript received: March 29, 2024
Revised manuscript received: June 27, 2024
Accepted manuscript online: July 10, 2024
Version of record online: October 2, 2024